Plasmon-Resonant Nanoparticles and Nanostars with Magnetic Cores: Synthesis and Magnetomotive Imaging

Hyon-Min Song, Qingshan Wei, Quy K. Ong, and Alexander Wei*

Department of Chemistry, Purdue University, 560 Oval Drive, West Lafayette, Indiana 47907-2084

ARTICLE

ABSTRACT Plasmon-resonant gold nanostars (NSTs) with magnetic cores were synthesized by a multistep sequence from superparamagnetic Fe_3O_4 nanoparticles (NPs) and evaluated as optical contrast agents under magnetomotive (MM) imaging conditions. Core—shell Fe_3O_4@Au NPs were prepared in nonpolar organic solvents with nanometer control over shell thickness and with good epitaxy to the Fe_3O_4 surface. Anisotropic growth was performed in micellar solutions of cetyltrimethylammonium bromide (CTAB) under mildly reducing conditions, resulting in NSTs with physical features similar to those produced from colloidal gold seeds. NSTs could be produced below 100 nm from tip to tip, but seed size had a significant impact on growth habit, with larger seed particles producing submicrometer-sized "morning stars". Both NSTs and aggregated core—shell NPs are responsive to in-plane magnetic field gradients and can provide enhanced near-infrared (NIR) contrast under MM conditions, but do so by different mechanisms. NSTs can modulate polarized NIR scattering with minimal translational motion, giving the appearance of a periodic but stationary "blinking", whereas core—shell NP aggregates require lateral displacement for signal modulation. The polarization-sensitive MM imaging modality offers the dual advantage of enhanced signal quality and reduced background signal and can be applied toward the detection of magnetomotive NSTs in heterogeneous biological samples, as illustrated by their detection inside of granular cells such as macrophages.

KEYWORDS: imaging · magnetic nanoparticles · nanomedicine · nanostars · plasmonics · synthesis

Nanomedicine, broadly defined as the application of nanoscale materials and measurements toward problems of biomedical importance, has also become a driving force for new concepts in nanoscience and technology. A substantial fraction of this activity is focused on the development of multifunctional nanoparticles (NPs) that can enhance or introduce unique modalities in biomedical imaging, with the extra potential of combining imaging with therapeutic action (aka theranostics). Two types of NPs with particular promise as theranostic agents are plasmon-resonant colloidal Au particles and superparamagnetic iron oxide (Fe_3O_4) particles, both of which are under active investigation for clinical applications.[1] Au NPs can be prepared in anisotropic forms to support large optical cross sections at near-infrared (NIR) wavelengths and are favored in optical imaging modalities for their high transmittivity through biological tissues. Fe_3O_4 NPs are useful as T_2-weighted contrast agents in magnetic resonance imaging (MRI) and can respond to magnetic field gradients for applications requiring site-specific localization (*e.g.*, magnetofection) or separations (*e.g.*, cell sorting). Plasmon-resonant and magnetic NPs can also mediate localized hyperthermic effects, and their applications toward tumor cell thermolysis and tissue ablation are now well-documented.[1,2]

The integration of magnetic and plasmonic functions into a single platform has obvious benefits for nanomedicine applications and has been the objective of several novel developments in multifunctional NPs.[3−10] We were interested in the possibility of combining polarization-sensitive plasmons with magnetomotive activity to support dynamic modes of optical imaging, as a mechanism for countering the intrinsically high scatter in biological tissues. This concept has recently materialized in the demonstration of gyromagnetic imaging, a dynamic modality based on the periodic scattering behavior of Au nanostars (NSTs) containing magnetic cores.[11] The novelty of gyromagnetic imaging originates from the NSTs' polarization-sensitive plasmon modes, which support a periodic modulation in NIR scattering intensity while gyrating in response to a rotating magnetic field gradient. The spatiotemporal data can be transformed into frequency-selective images with a drastic reduction in background noise, enabling NSTs to be detected against a field of brighter but aperiodic scatterers.

Ⓜ This paper contains enhanced objects available on the Internet at http://pubs.acs.org/journals/ancac3.

*Address correspondence to alexwei@purdue.edu.

Received for review May 29, 2010 and accepted July 29, 2010.

Published online August 6, 2010. 10.1021/nn101202h

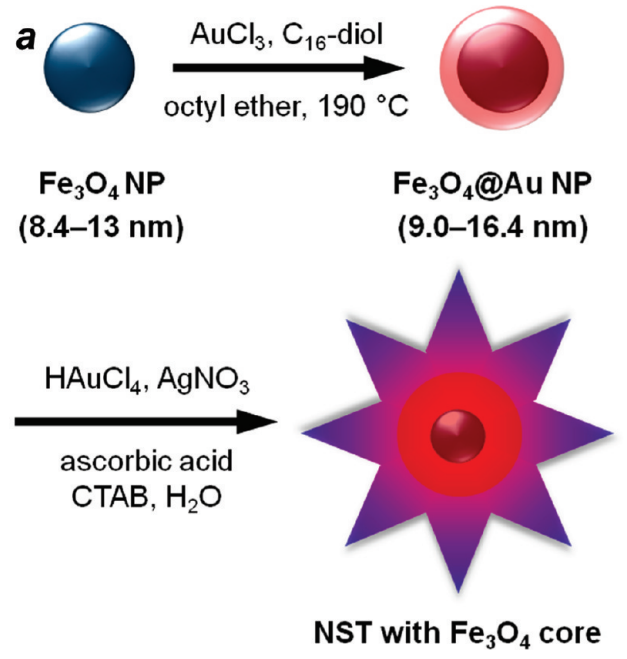

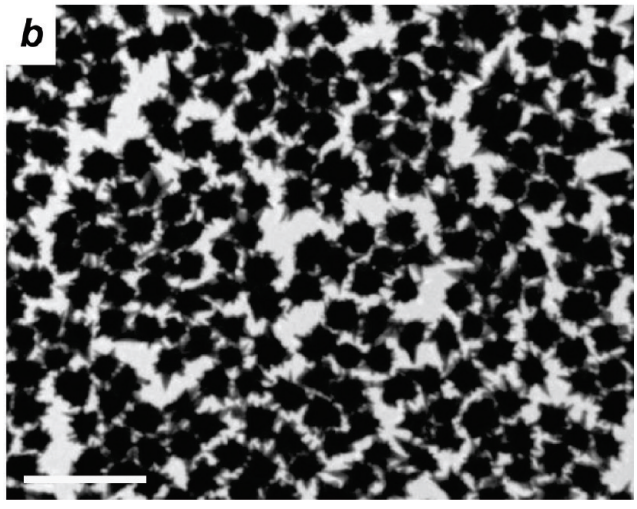

Figure 1. (a) Synthetic scheme of Au nanostars (NSTs) with Fe_3O_4 cores; (b) TEM image of NSTs. Bar = 500 nm.

Here we present a multistep synthesis of Au nanostars with Fe_3O_4 cores, with a systematic examination of the factors affecting the outcome of the final structures (Figure 1). Fe_3O_4 NPs are converted into core−shell Fe_3O_4@Au NPs under solvothermal conditions with nanometer control over shell thickness,[12−16] followed by the seeded growth of NSTs in aqueous micellar solutions of cetyltrimethylammonium bromide (CTAB) with good responsivity to low magnetic field gradients ($B \sim 60$ G). The micellar conditions of the latter step are widely used in the synthesis of anisotropic Au NPs such as NSTs and nanorods, but the size of the core−shell NP seeds is critical in determining the shape and size of the final nanostructures.

With respect to optical contrast, NSTs and other magnetomotive particles are able to support dynamic modes of optical imaging based on their response to linear (in-plane) magnetic field gradients, generated simply by periodic cycles of on−off switching. Magnetomotive (MM) imaging using transverse field gradients is complementary to but distinct from gyromagnetic imaging, whose contrast is generated by rotating magnetic field gradients.[11] We elected to develop MM imaging based on polarized scattering, using a standard optical microscope and a broad-band excitation light source. Contrast is enhanced by combining technological advances in image data collection with Fourier-based signal processing, while keeping hardware requirements as simple and low-cost as possible. In this study, we show that both NSTs and core−shell NPs can be applied toward dynamic optical imaging but differ in their responses to in-plane field gradients, with subsequent impact on their mechanisms for generating magnetomotive contrast.

RESULTS AND DISCUSSION

Synthesis of Core−Shell Au@Fe_3O_4 Nanoparticles. Iron oxide nanoparticle seeds (4.3 ± 0.5 nm) were prepared in octyl ether by the reduction of Fe(III)(acetylacetonate)$_3$ with 1,2-hexadecanediol in the presence of oleylamine and oleic acid, using the methods developed by Sun and co-workers.[17,18] These were isolated by precipitation with ethanol and resubjected to similar reaction conditions to produce larger iron oxide NPs. Adjusting the amounts of oleylamine and oleic acid resulted in uniform particles with diameters up to 12.8 nm (Figure 2a) and were visibly responsive to weak magnetic field gradients ($B \sim 60$ G). High-resolution transmission electron microscopy (HRTEM) of the larger NPs revealed most of these to be single crystals, with lattice planes along the (111) and (110) directions (Figure 2b). Selected area electron diffraction (SAED) and powder X-ray diffraction (XRD) produced patterns corresponding to an inverse spinel structure having a face-centered cubic (fcc) phase (space group *Fd*3*m*), with a cell parameter of 8.4052 Å as obtained by Rietveld refinement (Figure 2c,d). This value matches well against that of bulk fcc-Fe_3O_4 (JCPDS 79-0418; $a = 8.3985$ Å). Furthermore, heating Fe_3O_4 NPs at 500 °C for 12 h under an inert atmosphere did not induce any significant changes in diffraction pattern (Figure S1, Supporting Information), whereas colloidal γ-Fe_2O_3 (obtained from commercial sources) experienced a phase transition to α-Fe_2O_3, as characterized by XRD. This supports earlier claims that the iron oxide particles made by this route are composed mostly of Fe_3O_4.[17]

Core−shell Fe_3O_4@Au NPs were synthesized from freshly prepared Fe_3O_4 particles by treatment with $AuCl_3$ at room temperature followed by heating to 190 °C in octyl ether for 90 min, adapting the conditions developed by Zhong and co-workers for smaller (<6 nm) Fe_3O_4 NPs.[13] Ultrathin Au shells were formed using Au/Fe mole ratios between 2 and 3.3; TEM size analysis indicated shell widths ranging from an atomic layer of Au on 8.4 nm Fe_3O_4 cores to 1.3 nm shells of Au on 12.8 nm Fe_3O_4 cores (see Table 1). Interestingly, attempts to grow thicker (>2 nm) shells resulted in less uniform growth, with relative standard deviations in particle size of over 10%; the thicker shells also had an adverse effect on subsequent nanostar growth (see below). It is worth mentioning that thicker Au shells have been grown around colloidal Fe_3O_4 particles by the physisorption of small Au nuclei, followed by electroless deposition.[19−21]

HRTEM analyses of individual Fe_3O_4 and core−shell NPs suggest a favorable epitaxy between lattice planes in the Fe_3O_4 core and the Au shell (Figure 3). The measured (222) spacings of nanocrystalline Fe_3O_4 (d = 2.45 Å, Figure 2b) are within 3% of the (111) spacings of Au in the core−shell NPs (d = 2.37−2.42 Å) and also close to that measured in bulk Au (JCPDS 04-0784; d = 2.35 Å). Similarly, the measured (220) spacings of Fe_3O_4 (d = 2.97 Å) are within 3% of the (110) spacings of Au (d = 2.88 Å), measured in both core−shell NPs and bulk Au. HRTEM analysis of the Au shell also reveals twinned defects at the boundary of two (111) lattice planes (Figure 3c). Twinning is well-known to reduce surface energy strain and can promote the formation of (111) planes, which are strongly favored in the growth of Au nanostructures.[22]

Both TEM and powder XRD analyses indicate the growth habit of the Au shell to be essentially isotropic, with an increase in shell thickness corresponding to a sharpening of the XRD peaks (see Figures 4 and S2, Supporting Information). As noted previously, the Fe_3O_4 phase enveloped within the Au shell is hardly detectable.[13,14] Indeed, the X-ray scattering from Au completely dominates the XRD spectrum, even in the case of Fe_3O_4@Au NPs with shell thicknesses corresponding to a single atomic layer (Figure 4b. While the XRD peaks of the core−shell NPs match well with that obtained from bulk Au, their line widths belie the thicknesses of the ultrathin Au shells. Applying the Debye−Scherrer equation to the (111) peaks ($D = 0.9\lambda/\beta \cos\theta$, where λ is the X-ray wavelength for Cu Kα (1.5406 Å) and β is the fwhm in radians) produces effective grain sizes ranging from 4.5 to 12.4 nm, less than the overall particle diameters (9.0−16.4 nm) but much larger than the shell thicknesses (0.3−2.0 nm) estimated by HRTEM (Table 1). The fact that the Scherrer values are lower than the particle diameters is expected, considering the intrinsic heterogeneity of

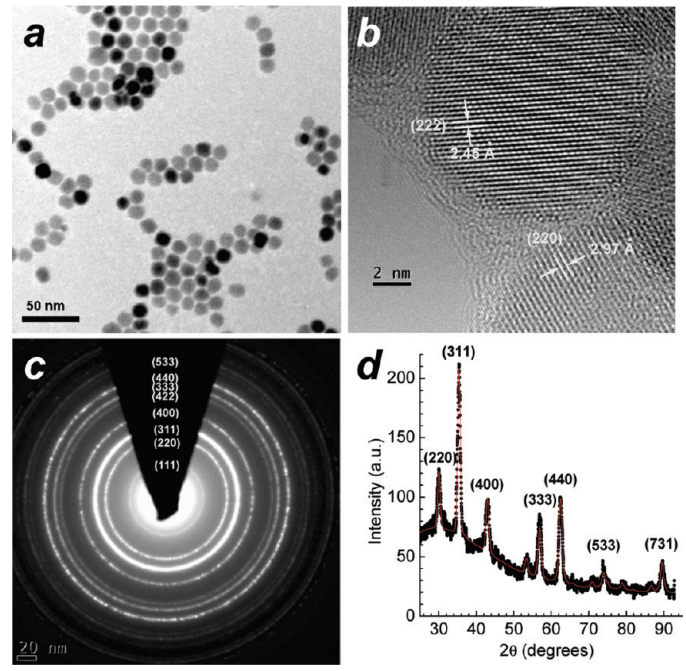

Figure 2. (a,b) TEM and HRTEM analysis of 12.8 ± 0.9 nm Fe_3O_4 NPs; (c,d) SAED and powder XRD pattern with Rietveld refinement (in red).

the core−shell system. On the other hand, it is remarkable that these values are so much larger than the shell thicknesses, a possible indication of the close epitaxial relationship between the (111) lattice planes in the Au shell and the underlying Fe_3O_4 core.

At first glance, the small lattice mismatch between the lattice parameters of Fe_3O_4 and fcc-Au (<3%) suggests a heteroepitaxial mechanism for core−shell growth, similar to that described for binary Fe_3O_4/Au nanostructures.[4,7] However, the direct application of electroless Au deposition onto larger Fe_3O_4 NPs (>16 nm) does not yield core−shell structures, although the chemistry is essentially identical to that used with smaller Fe_3O_4 NPs. A recent study involving the deposition of Au onto planar Fe_3O_4(111) substrates indicates that, while heteroepitaxy is favorable, the gain in adhesion energy is insufficient to promote total monolayer coverage and does not prevent the formation of 3D Au islands with lower surface area.[23] This suggests that the

TABLE 1. TEM and Debye−Scherrer Analysis for Core−Shell Fe_3O_4@Au NPs

	TEM size analysis[a]			XRD (Scherrer analysis)[b]	
entry	d_{core} (nm)	d_{shell} (nm)	t_{shell} (nm)	β (rad)	D (nm)
1	8.4 ± 1.1	9.0 ± 0.9	0.3	0.033	4.5
2	9.5 ± 0.7	11.9 ± 1.3	1.2	0.020	7.3
3	12.8 ± 0.9	15.4 ± 1.3	1.3	0.014	10.8
4	12.5 ± 1.0	16.4 ± 1.9	2.0	0.012	12.4

[a]Based on minimum particle count (N) of 100; see Figure 2. [b]Based on (111) peaks in Figures 4 and S2 (Supporting Information).

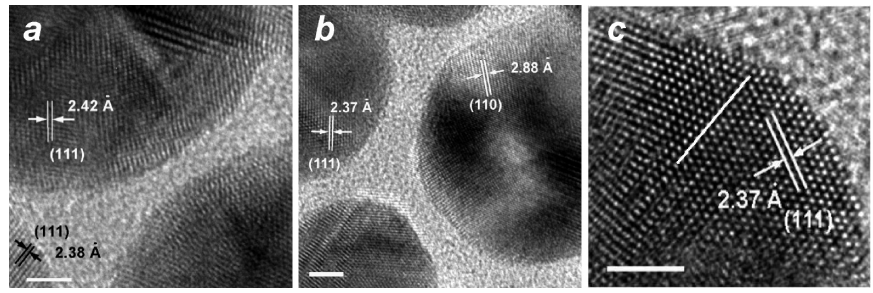

Figure 3. HRTEM analysis of core−shell Fe_3O_4@Au NPs (15.4 ± 1.3 nm). (a,b) Lattice planes of Au shell indicates growth in both the (111) direction (d = 2.37−2.42 Å) and the (110) direction (d = 2.88 Å). (c) Twinned defect at the boundary of two (111) lattice planes (white line). Bar = 2 nm.

growth of ultrathin Au shells around Fe_3O_4 NPs is not simply driven by favorable heteroepitaxy and requires further study to elucidate the basis for such fine control over shell thickness.

Synthesis of Au Nanostars with Magnetic Cores. Methods for producing stellated or hyperbranched gold nanostrutures have been described previously, using either a direct "one-pot" synthesis[24−29] or by seeded growth.[30−35] The Au NP seeds can be prepared in either aqueous solutions or in organic solvents, and additives can be introduced to increase the branching of the final nanostructures. In this study, we used the Fe_3O_4@Au NPs described above to seed the growth of NSTs in aqueous, micellar CTAB solutions, a condition well-known to promote anisotropic growth.[30,33]

NSTs were synthesized by dispersing Fe_3O_4@Au NPs in 2.5 mM sodium citrate (*ca.* 4 mg/mL), followed by their injection into a growth medium composed of CTAB, $HAuCl_4$, $AgNO_3$, and ascorbic acid (Figure 5a−c). The growth of NSTs was essentially complete within 15 min, and the final nanostructures were stable for at least a month at room temperature, following the removal of excess CTAB (see below). HRTEM analysis along individual NST spines revealed the presence of multiple twinning defects and overall growth along the (111) direction, similar to that observed in previous analyses.[36] Extinction spectra were characterized by strong NIR bands with a shoulder starting from 700 nm, corresponding to the NSTs' anisotropic projections.[37] The Fe_3O_4 core had minimal influence on the optical properties of the NSTs, which was confirmed by a comparison with NSTs generated from citrate-stabilized colloidal Au seeds (see Supporting Information). However, the initial concentration of $HAuCl_4$ was important for generating multipodal NSTs with NIR activity. A several-fold reduction in Au ion concentration resulted in fewer projections and lower anisotropy, with extinction bands centered around 650 nm (Figure 5d,e).

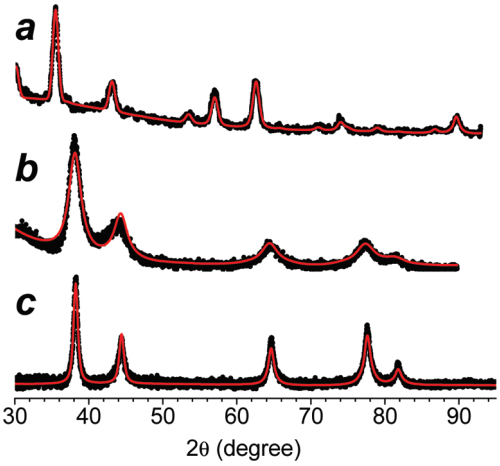

Figure 4. XRD spectra as a function of Au shell thickness, with Rietveld refinements. (a) Fe_3O_4 NP (d = 12.8 nm) without Au shell; (b) core−shell NP with 0.3 nm Au shell (Table 1, entry 1); (c) core−shell NP with 2.0 nm Au shell (Table 1, entry 4).

It is important to note that hyperbranched growth is highly sensitive to the preparation of the growth solution and also to seed dispersion conditions. With respect to the growth solution, we found that the sequential addition of $HAuCl_4$ and ascorbic acid to the CTAB/$AgNO_3$ mixture, with a short (15 min) induction period between additions, gave the most reproducible results. Adding ascorbic acid immediately after $HAuCl_4$ resulted in smaller NPs and fewer star-shaped particles, whereas adding seed particles immediately after ascorbic acid resulted in a lower overall yield. With respect to dispersion conditions, the use of citrate-stabilized Fe_3O_4@Au NPs resulted in the growth of multipodal structures, whereas Fe_3O_4@Au NPs stabilized in CTAB solutions produced essentially isotropic NPs under identical conditions. The difference in growth habit is obvious upon visual inspection: suspensions of NPs generated from CTAB-stabilized seed particles appear wine-red with a relatively narrow plasmon resonance band close to 550 nm, whereas suspensions of NSTs produced under optimized growth conditions appear dark blue with transmitted light but brownish-orange under scattering conditions, with extinction bands in both the visible and NIR regions (Figure 5c). These observations are in accord with an earlier study by Hafner and co-workers,[33] in which CTAB-

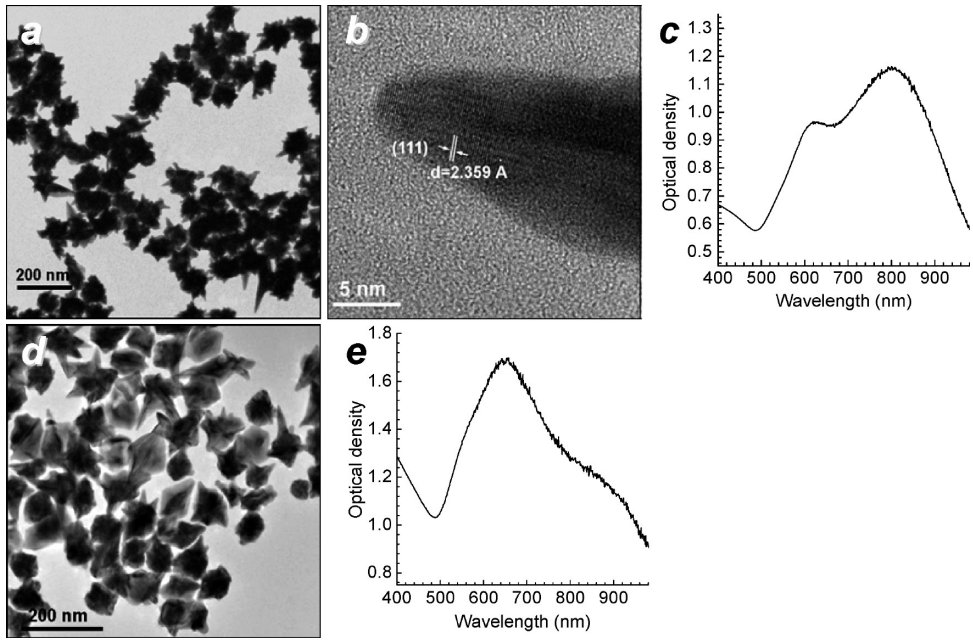

Figure 5. (a,b) TEM image and HRTEM analysis of Au NSTs with Fe_3O_4 cores grown from citrate-stabilized Fe_3O_4@Au NPs; $[HAuCl_4] = 7.8$ mM. (c) Extinction spectrum of NSTs, with bimodal maxima at 620 and 800 nm. (d,e) TEM image and extinction spectrum of anisotropic particles grown from citrate-stabilized Fe_3O_4@Au NPs; $[HAuCl_4] = 2.1$ mM.

stabilized Au NPs ($d \sim 10$ nm) were far less effective at inducing anisotropic growth. Unlike the case of Au nanorods, in which small (<4 nm) Au nanoparticle seeds are presumed to have a relatively high density of twin defects for initiating rapid growth, the NPs used to seed NST growth are covered predominantly by (111) facets. Given the lower density of twinning defects in these larger seed particles, anisotropic growth may be effectively inhibited by saturating these sites with surface-active agents, such as CTAB, before their exposure to the growth solution.

The anisotropic radial growth step also appears to have a temporal component. Core−shell NPs with thicker Au coatings ($t_{shell} \sim 7$ nm) typically generated submicrometer-sized particles coated with short spines, reminiscent of spiked mace heads or flails used in medieval combat (Figure 6). The low aspect ratios (projection length *versus* particle diameter) featured in such "morning star" particles indicate a two-stage growth process: an induction period dominated by rapid, autocatalytic growth, followed by kinetically controlled deposition at twin boundaries along local (111) axes. The growth of these projections at a late stage implies that (i) twinning defects are constantly being generated at the particle surface during the isotropic growth stage and (ii) as overall growth rates decrease due to consumption of $HAuCl_4$, deposition at twin boundaries with net growth in the (111) direction becomes the dominant growth mechanism. Preferential growth along twinning planes is well-known to minimize strain energy and is sufficient to explain the final outcome, although surface passivation is likely also important for stabilizing the higher energy surfaces featured in anisotropic nanostructures.[38]

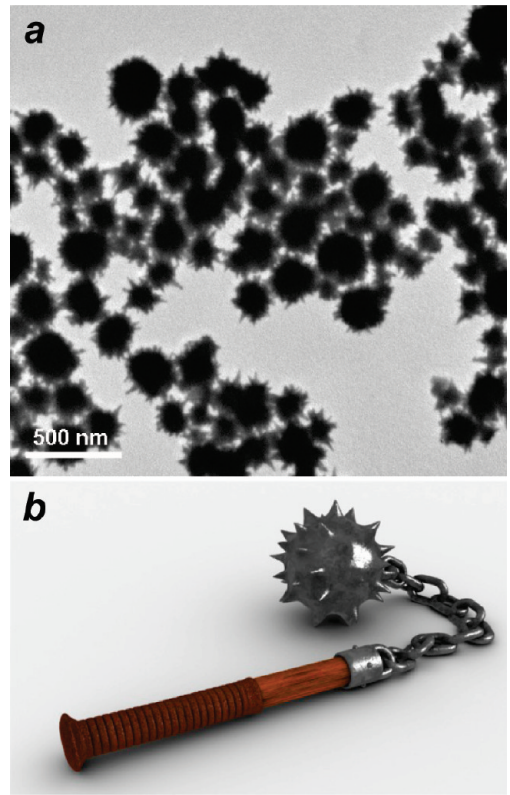

Figure 6. (a) TEM image of morning star particles ($d_{av} > 200$ nm), grown from 27 nm core−shell Fe_3O_4@Au NPs. (b) Model of a morning star flail.

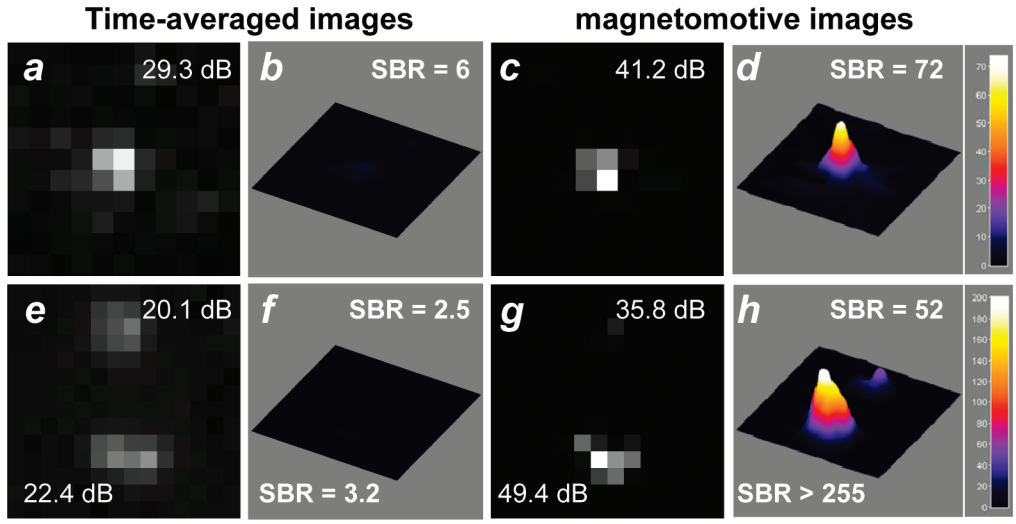

Figure 7. Polarized dark-field imaging of NSTs on polymer-coated glass slides under magnetomotive conditions (100× objective; 1 pixel = 226 nm). (a−d) Time-averaged image of single NST using 780 nm laser excitation *versus* ω-filtered MM image of NST at 780 nm (6000 frames, ω = 5 Hz). Peak SNR is enhanced by 11.9 dB and SBR by 12. (e−h) Time-averaged and ω-filtered MM images of NSTs using a broadband source with long-pass filter ($\lambda_{ex} > 650$ nm). Peak SNRs for upper and lower NST are enhanced by 15.7 and 27.0 dB, respectively; SBR by 20 and over 80. Bar = 3 μm.

Ⓦ See video of blinking NSTs at 5 Hz.

Magnetomotive Imaging of Plasmon-Resonant Nanostars and Core−Shell Fe_3O_4@Au Nanoparticles. Several examples of hybrid magnetic−plasmonic nanostructures with NIR activity have been reported, with the rationale of using the magnetic component for separations or MRI contrast.[3−10] As we and others have shown, hybrid nanostructures can also support novel, dynamic modes of optical imaging driven by magnetic field gradients.[11,39] Magnetomotive (MM) imaging modalities have been developed for optical coherence tomography (OCT), based on field-induced perturbations in the morphology-dependent scattering of tissues impregnated with magnetic NPs,[40,41] and may be further utilized for evaluating the mechanical properties of the embedding materials, based on their viscoelastic responses to applied magnetic fields.[42−44]

MM imaging has the singular advantage of enabling image analysis in the frequency domain, with a substantial reduction in both noise and background level. Pixelated data collected in the time domain can be subjected to Fourier transform (FT) and filtered at a specific frequency to generate images with dramatically enhanced contrast.[11] Frequency-filtered MM imaging of cells labeled with core−shell Fe_3O_4@Au nanoparticles has been performed at visible wavelengths, using a magnetomotive force oscillating at a low driving frequency ($\omega < 2$ Hz).[39] We recently demonstrated the enhanced NIR detection of individual NSTs by gyromagnetic imaging, using a magnetically induced torque to modulate the amplitude of polarized scattering at twice the driving frequency (2ω).[11] Under these conditions, the in-plane motion of NSTs is barely noticeable in most cases, giving the appearance of a periodic but stationary "twinkling".

In this study, we use in-plane magnetic pulses to produce frequency-selective optical contrast. An electromagnet operating with a 50% duty cycle at a low driving frequency (1−20 Hz) was used to generate transient magnetic field gradients ($B \sim 60$ G) during the collection of polarized NIR scattering from NSTs on polymer-coated glass slides (see Experimental Section). Periodic modulations in scattering amplitude or "blinking" were recorded as digitized images (800−7200 frames, collected up to 125 fps), then subjected to FT to produce ω-filtered images of high quality. MM contrast can be generated using either a 780 nm solid-state laser for incident illumination (Figure 7a−d) or an inexpensive white light source equipped with a long-pass filter ($\lambda >$ 650 nm, Figure 7e−h), with peak signal-to-noise ratios (SNR) typically in the range of 30−50 dB and signal-to-background ratios (SBR) in the tens to hundreds, based on the video recording conditions for this study. The same NSTs were also subjected to gyromagnetic imaging conditions using the same optical workstation and a rotating field gradient of 80 G,[11] which yielded 2ω-selective images of comparable quality and contrast as those obtained through ω-selective MM imaging. However, we note that the signals generated by NSTs under gyromagnetic conditions are more uniform, for reasons to be discussed below.

It should be noted that peak SNR and SBR values are related but have different meanings. Peak SNR is

commonly used to evaluate signal quality, whereas SBR is more practical for evaluating image contrast. In this study, their values are derived simply as

$$\mathrm{SNR(dB)} = 20 \times \log\left(\frac{A_{\mathrm{NST}} - A_{\mathrm{bk}}}{\sigma_{\mathrm{bk}}}\right) \quad (1)$$

$$\mathrm{SBR} = \frac{A_{\mathrm{NST}}}{A_{\mathrm{bk}}} \quad (2)$$

where A_{NST} and A_{bk} represent the mean intensities of pixel values corresponding to peak signal and a selected background region (60 pixels on average), and σ_{bk} is the standard deviation of A_{bk}.[11]

The initial SNR and SBR values in time-averaged images using NIR laser illumination (prior to FT) are already quite good due to low background (Figure 7a,b), so enhancements by MM imaging can be relatively modest with an increase in SNR by 12 dB and a 10−20-fold increase in SBR. On the other hand, NSTs imaged using broad-band illumination (Figure 7e,f) suffer from higher noise levels, with signals close to the limit of acceptable quality and contrast (SNR = 20−22; SBR = 2.5−3.0). These weak signals are dramatically enhanced under MM imaging conditions, with improvements in SNR of up to 27 dB and in SBR by as much as 2 orders of magnitude (Figure 7g,h). Therefore, MM imaging can be particularly effective for enhancing the detection of weak signals in noisy environments.

The MM contrast mechanism in Figure 7 is primarily based on torque-induced amplitude changes in polarized scattering, driven by the reorientation of the core's magnetic moment in the direction of the applied field. Lateral displacements of NSTs induced by in-plane field switching are typically at the resolution limit of the imaging conditions (0.23 μm/pixel) and are not a requirement for signal modulation. Furthermore, while some variability in amplitude modulation exists between NSTs, the time-averaged (rms) intensity of each scatterer is essentially constant over the duration of the imaging experiment. This suggests that (i) NSTs adopt bistable states in response to magnetomotive switching, and (ii) the NIR-active plasmon modes of each state are differentially aligned with respect to the polarization plane (Figure 8). It should be noted that the Fe_3O_4 core is roughly spherical and its magnetization is not associated with the structural anisotropy of the NST, meaning that MM imaging does not require a correlation between the radial plasmon mode and the magnetic easy axis, similar again to gyromagnetic imaging.[11] Therefore, a switch in plasmon orientations is sufficient for a significant change in polarized scattering.

The modulation of polarized scattering between on/off states (*i.e.*, states 1 and 2) is periodic for the majority of MM-active NSTs, as is evident in the

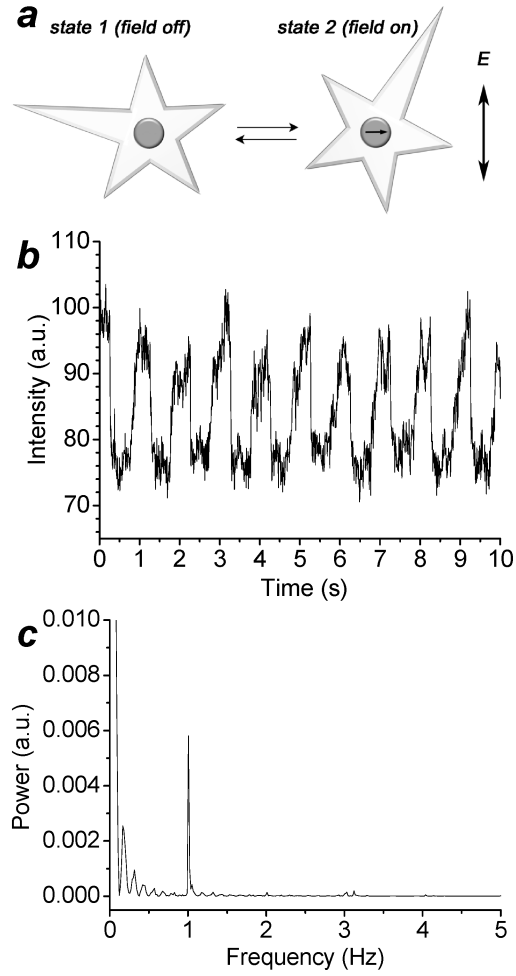

Figure 8. Generation of magnetomotive contrast from polarization-sensitive NSTs. (a) Bimodal orientation of NST spine with NIR-active (radial) plasmon mode in response to in-plane magnetic field gradient (on/off states), accompanied by a change in polarized scattering intensity. No correlation is assumed between plasmon dipole and magnetic easy axis. (b) Periodic modulation in polarized scattering from single NST responding to a driving frequency of 1 Hz. (c) Power density spectrum of MM scattering, with a characteristic peak at 1 Hz.

ω-selective signal generated by NIR laser irradiation (Figure 8c). The field-induced reorientation of the NSTs is thus countered by a commensurate restoring force, most likely mediated by an elastic adhesion to the substrate. However, contrast enhancement by this mechanism is not as uniform as that generated under gyromagnetic conditions, either in terms of overall response rate (roughly half of the NST population) or on an individual basis. We attribute this in part to variations in NST orientation: the MM signal can be weakened if the NIR-active plasmon mode is not adequately aligned to produce periodic changes in polarized scattering. Bimodal stability is also important, as local viscoelastic effects may cause deviations from periodic motion, resulting in anharmonic signal oscillations (see below). An example of such variability in MM response

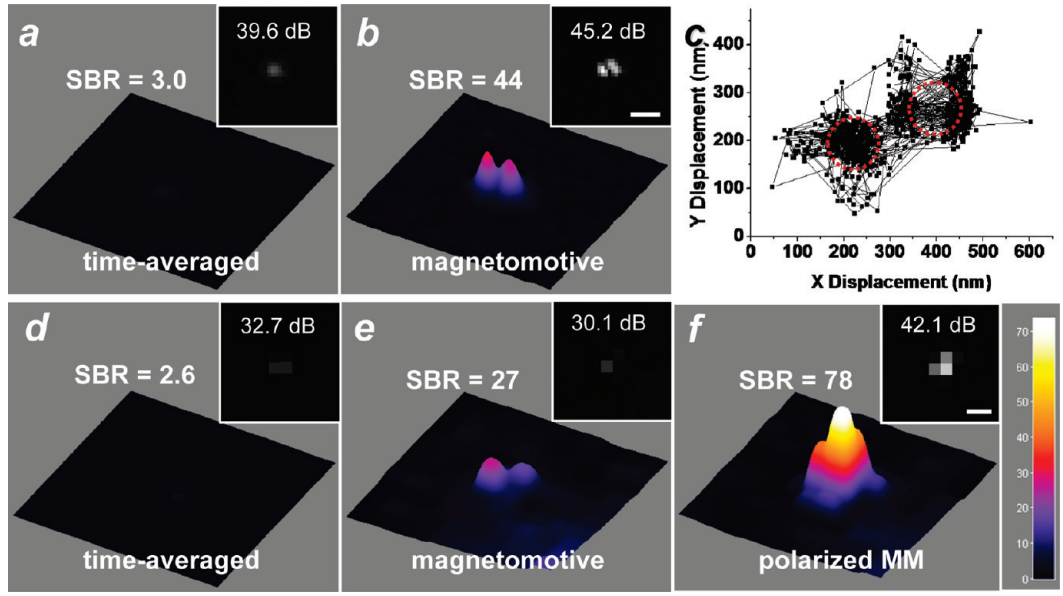

Figure 9. Dark-field magnetomotive imaging based on lateral particle displacement. (a,b) Contour plots of time-averaged *vs* ω-filtered MM images of magnetic core−shell NPs, with SBR values ($\lambda_{ex} > 650$ nm, 800 frames, $\omega = 1$ Hz). Two-dimensional images shown as insets, with SNR values; bar = 1 μm. (c) Trajectory of MM particles in response to in-plane field gradient, with centroids outlined in red. (d,e) Contour plots of time-averaged *vs* ω-filtered MM images of NST without polarization, with SBR values ($\lambda_{ex} > 650$ nm; 6000 frames, $\omega = 1$ Hz). (f) MM image of NST with polarization; 2D images are shown as insets, with SNR values; bar = 1 μm.

Ⓦ See the video for particle tracking of core−shell NPs.

is shown in Figure 7e−h: while both NSTs produce strong NIR signals, the fluctuations in polarized scattering from the upper NST are only weakly periodic when exposed to an in-plane field gradient ($\omega = 1$ Hz), resulting in lower (but still respectable) signal quality under MM imaging conditions. It is interesting to note that the MM signal from the upper NST is actually reduced, but the SNR is higher by virtue of the reduction in background.

The modulation of polarized scattering from magnetomotive NSTs by in-plane field gradients raises the question whether other types of hybrid nanoparticles can enhance optical signals using a similar mechanism. We thus examined the generation of MM contrast by Fe_3O_4@Au core−shell NPs, which can exhibit significant NIR scattering upon aggregation due to strong plasmon coupling.[45−47] The core−shell NPs do not exhibit any significant changes in polarized NIR scattering under MM conditions; however, significant contrast enhancement may be generated based on the detection of in-plane motion (Figure 9a,b). Optical polarization is unnecessary for signal modulation in this case, but instead requires a minimum displacement in the time domain.[39] Particle tracking analysis suggests a threshold of approximately half a pixel, close to 200 nm under our imaging conditions (Figure 9c). The MM image confirms that the lateral displacement is bimodal, with a nearly 15-fold enhancement in SBR relative to the time-averaged image, but provides only a modest improvement to SNR.

It is worth noting that some NSTs are also capable of producing MM contrast *via* lateral displacement (Figure 9d,e), but the signal density is lower and the contrast enhancement is less than that observed with polarization-sensitive MM imaging (Figure 9f). The latter not only boosts SBR 3-fold but also improves SNR by 10−12 dB. Therefore, whereas MM imaging provides contrast enhancement by suppressing background noise, additional signal enhancement is achieved by using ω-filtered polarization.

To demonstrate how polarization-sensitive MM imaging might operate in a biological setting, *in vitro* experiments were performed using albumin-coated NSTs internalized by macrophages. CTAB-stabilized NSTs were first cleansed by treatment and centrifugation with polystyrenesulfonate (proven recently to be a useful detergent for removing CTAB from Au nanorods),[48] then resuspended in a 1% solution of bovine serum albumin (BSA; see Experimental Section). Adherent RAW 264.7 cells (an immortalized line of murine macrophages) were incubated with BSA-coated NSTs to initiate macrophagocytosis and periodically monitored over a period of 24 h. NSTs with magnetomotive activity were most abundant a few hours after NST uptake, but the number of field-responsive particles decreased over time even though the particle uptake increased overall (Figure 10a). This effect can be attributed to the gradual immobilization of NSTs encapsulated within late-stage phagosomes and lysosomes, which typically form physical attachments to the cytoskel-

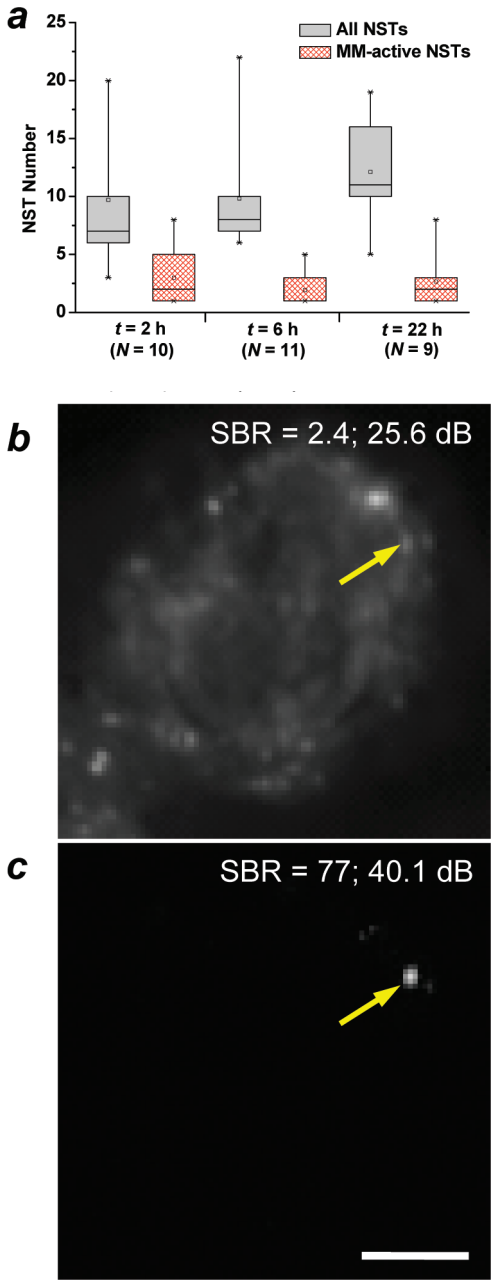

Figure 10. (a) Macrophage uptake of BSA-coated NSTs (t = 2−22 h). The fraction of MM-active NSTs decreases over time, despite an overall increase in NST uptake. (b,c) Time-averaged *vs* ω-filtered MM images of internalized NSTs after 22 h, with SBR and SNR values ($\lambda_{ex} > 650$ nm, 800 frames, $\omega = 1$ Hz); bar = 5 μm.

etal framework at the end of the endocytotic process.[49,50] The immobilized NSTs can no longer be visualized directly by MM imaging regardless of their scattering intensities, as their signals are effectively edited by Fourier transform.

Internalized NSTs that are still capable of responding to in-plane field gradients can be imaged with enhanced contrast under MM conditions and are readily distinguished against a field of aperiodic scatterers. This includes secretory vesicles and other intracellular granules, many of them presumably labeled with immobilized NSTs. In the example shown in Figure 10b,c, the peak SNR and SBR of a magnetomotive NST signal after polarization-sensitive MM imaging are 40.1 dB and 77, respectively, in accord with the contrast enhancement generated under abiotic conditions. When compared with the corresponding time-averaged image, SNR improved by 15 dB and SBR by over 30-fold.

In closing, nanoparticles with hybrid magnetic and plasmonic properties can serve as contrast agents for dynamic imaging modalities based on optical scattering. Au nanostars with Fe_3O_4 cores are particularly well-suited for this function as they support polarization-sensitive modes of magnetomotive imaging, enabling them to stand out against the heterogeneous field of scattering bodies that are omnipresent in biological cells and tissues. While our application of MM imaging has focused on the enhancement of signals derived from scattering, we note that dynamic mechanisms of contrast generation offer a general approach for enhancing optical signal and image contrast and can be applied toward imaging methods based on fluorescence, multiphoton luminescence, or fluorescence resonance energy transfer (FRET).[1,2,51,52] The detection of NSTs in granulated cells such as macrophages raises some interesting possibilities of correlating local magnetomotive activities with biomechanical processes within the cell. In particular, MM contrast agents are sensitive to changes in their microenvironment, as illustrated by the gradual loss of magnetomotive signals during macrophage uptake. This implies an interplay between internalized NSTs and the cytoskeletal network, with potentially significant effects in cell physiology; such studies are currently in progress.

EXPERIMENTAL SECTION

Chemical Synthesis. All chemicals and solvents were obtained from commercial sources and used without further purification unless otherwise stated. Deionized water with a measured resistivity above 18 MΩ · cm was obtained using an ultrafiltration system (Milli-Q, Millipore) and passed through a 0.22 μm filter for removal of particulate matter. Monodisperse batches of 4 and 13 nm Fe_3O_4 NPs were prepared according to the methods described by Sun;[17,18] core−shell Fe_3O_4@Au NPs and NSTs were prepared by modifying the procedures described by Zhong and Hafner, respectively.[13,33] The Au/Fe mole ratio used in the core−shell NP synthesis varied between 2 and 3.3, for shell thicknesses between 0.3 and 1.3 nm (see Table 1 and Supporting Information for TEM-based size analyses).

NSTs were generated from Fe_3O_4@Au core−shell NPs at room temperature using a seeded growth method, similar to the synthesis of pure Au NSTs.[33] A typical seed solution was prepared by dispersing 2 mg of Fe_3O_4@Au core−shell NPs in 500 μL of 2.5 mM sodium citrate, then sonicated for 20 min in an Eppendorf tube to produce a dark blue-brown solution. In a separate centrifuge tube, 5 mL of 0.2 M CTAB and 900 μL of 4 mM $AgNO_3$ were combined and also sonicated for 20 min to minimize

the formation of precipitates or the recrystallization of CTAB. The latter solution was treated with 5 mL of 7.8 mM $HAuCl_4$, then agitated with a vortex mixer for 15 s and allowed to stand for 15 min. Three hundred microliters of 78 mM ascorbic acid was added to this mixture, which was again agitated by vortex mixing and allowed to stand for 15 min. Finally, 250 μL of the seed solution was added to the growth mixture and mixed briefly by hand and left to stand at room temperature. The seeded solution initially appears brown by light scattering, but its optical transmittance becomes increasingly blue. The NST growth is essentially complete within 15 min of seed addition.

Physical Characterization. Optical extinction spectra (400−1000 nm) were measured using a Cary-50 spectrophotometer (Varian) with a 1 cm cell path length. X-ray diffraction (XRD) measurements were performed on dry powder samples with a Bruker D8-Focus diffractometer using Cu Kα radiation (20 kW, $\lambda = 1.54056$ Å) in $\theta-2\theta$ mode. Transmission electron microscopy (TEM) images were obtained with either a JEOL-2000FX using a LaB_6 filament at 200 kV or a Titan 80-300 (Tecnai) using a field-emission gun at 300 kV. TEM samples were prepared by drop-casting dilute solutions onto carbon-coated Cu grids: Fe_3O_4 and core−shell Fe_3O_4@Au NPs were dispersed in hexanes and allowed to evaporate in air, whereas NSTs were cast from aqueous suspensions and blotted after 20 min prior to drying. Fe_3O_4 and core−shell Fe_3O_4@Au NPs were prepared under an argon atmosphere.

Purification and Surface Treatment. CTAB-stabilized NSTs were first subjected to two cycles of centrifugation at 7300*g* for 20 min with redisperson in deionized water to remove excess surfactant. The concentrated suspension of NSTs was then treated with 1% PSS (70 kDa) for the exhaustive removal of CTAB, a protocol recently developed for the detoxification of Au nanorods.[48] A suspension of NSTs (1 mL, o.d. = 10) was treated with 1% PSS (20 μL) and agitated with a vortex mixer for 20 s, then allowed to stand for 2 h prior to centrifugation (same as above). The NSTs were resuspended in 10 mL of 0.01% PSS (100-fold dilution of 1% PSS solution) and subjected to a second round of centrifugation, then redispersed in 2 mL of 1% BSA in PBS with a vortex mixer to yield a stable suspension of BSA-coated NSTs.

Magnetomotive Imaging. A 10 μL aliquot of untreated NSTs or core−shell NPs was dropped onto a PSS-coated glass slide, then sealed with a coverslip. Scattering was recorded using an upright microscope (BX51WI, Olympus), equipped with a slide holder coupled to a dual optical fiber waveguide for quasi-darkfield illumination (Darklite Illuminator, MVI) and a digital camera rated for visible and NIR imaging (Rolera-XR, QImaging). A C-shaped electromagnet was positioned under the glass slide; the maximum field in the image plane was measured to be 60 G. A square-wave current was produced by a function generator (HP 33120A, Hewlett-Packard) with a frequency of 1−20 Hz (50% duty cycle) and further amplified by a power supply (BOP36-6DL, Kepco).

Magnetomotive imaging was performed using a 25 mW solid-state laser operating at 780 nm (B&W Tek) at a 60° angle of incidence or a halogen lamp with a long-pass filter ($\lambda > 650$ nm) for broad-band evanescent excitation through the supporting glass slide, with an optional polarization filter at the lamp source. NIR laser scattering was collected with a 40× objective lens; quasi-darkfield imaging was conducted using a 100× oil-immersion lens. Video recordings were performed at rates up to 123 fps.

Cell Uptake Studies. RAW 264.7 cells (derived from leukemic murine monocyte/macrophages) were cultured at 37 °C in a humidified atmosphere containing 5% CO_2. RAW cells were obtained from American Type Culture Collection and were cultured in Dulbecco's modified Eagle's medium (DMEM, BioWhittaker) with 10% fetal bovine serum (FBS, Sigma), 1% L-glutamine (200 mM, Sigma), and 1% penicillin−streptomycin (Invitrogen). Trypsinized cells were transferred to 6-well plates containing #0 coverslips (3 mL; 5×10^6 cells/mL) and incubated for 24 h in DMEM, then treated with an aliquot of BSA-stabilized NSTs (40 μL, o.d. = 4) with further incubation for up to 24 h. The coverslip with reattached cells was removed at specific time intervals and washed with PBS, then mounted onto a standard glass slide and sealed with nail polish. MM imaging of cells was performed using a 100× oil-immersion lens under quasi-darkfield conditions using polarized broadband illumination, as described above. All cell imaging studies were conducted within 2 h of slide mounting.

Acknowledgment. We thank J. Zimmerman of the Jonathan Amy Facility for Chemical Instrumentation (JAFCI) for construction of the low-frequency electromagnet. Support from the National Institutes of Health (RC1 CA147096) and the Purdue Research Foundation (research fellowship to Q.W.) is gratefully acknowledged.

Supporting Information Available: Additional characterization data for core−shell nanoparticles and nanostars (XRD analysis, TEM images, and size analysis); polarization-sensitive magnetomotive imaging of NSTs (video 1); magnetomotive imaging of lateral displacement of core−shell NPs (video 2). This material is available free of charge *via* the Internet at http://pubs.acs.org. ImageJ software can be obtained free of charge at http://rsb.info.nih.gov/ij.

REFERENCES AND NOTES

1. *Inorganic Nanoprobes for Biological Sensing and Imaging*, Mattoussi, H., Cheon, J., Eds.; Artech House: New York, 2009.
2. Tong, L.; Wei, Q.; Wei, A.; Cheng, J.-X. Gold Nanorods as Contrast Agents for Biological Imaging: Optical Properties, Surface Conjugation and Photothermal Effects. *Photochem. Photobiol.* **2009**, *85*, 21–32.
3. Yoon, T.-J.; Kim, J. S.; Kim, B. G.; Yu, K. N.; Cho, M.-H.; Lee, J.-K. Multifunctional Nanoparticles Possessing a "Magnetic Motor Effect" for Drug or Gene Delivery. *Angew. Chem., Int. Ed.* **2005**, *44*, 1068–1071.
4. Yu, H.; Chen, M.; Rice, P. M.; Wang, S. X.; White, R. L.; Sun, S. H. Dumbbell-like Bifunctional Au-Fe_3O_4 Nanoparticles. *Nano Lett.* **2005**, *5*, 379–382.
5. Lee, J.; Hasan, W.; Lee, M. H.; Odom, T. W. Optical Properties and Magnetic Manipulation of Bimaterial Nanopyramids. *Adv. Mater.* **2007**, *19*, 4387–4391.
6. Lim, J.; Eggeman, A.; Lanni, F.; Tilton, R. D.; Majetich, S. A. Synthesis and Single-Particle Optical Detection of Low-Polydispersity Plasmonic-Superparamagnetic Nanoparticles. *Adv. Mater.* **2008**, *20*, 1721–1726.
7. Wei, Y.; Klajn, R.; Pinchuk, A. O.; Grzybowski, B. A. Synthesis, Shape Control, and Optical Properties of Hybrid Au/Fe_3O_4 "Nanoflowers". *Small* **2008**, *4*, 1635–1639.
8. Wang, L.; Bai, J.; Li, Y.; Huang, Y. Multifunctional Nanoparticles Displaying Magnetization and Near-IR Absorption. *Angew. Chem., Int. Ed.* **2008**, *47*, 2439–2442.
9. Wang, C. G.; Chen, J.; Talavage, T.; Irudayaraj, J. Gold Nanorod/Fe_3O_4 Nanoparticle Nano-Pearl-Necklaces for Simultaneous Targeting, Dual-Mode Imaging, and Photothermal Ablation of Cancer Cells. *Angew. Chem., Int. Ed.* **2009**, *48*, 2759–2763.
10. Ma, L. L.; Feldman, M. D.; Tam, J. M.; Paranjape, A. S.; Cheruku, K. K.; Larson, T. A.; Tam, J. O.; Ingram, D. R.; Paramita, V.; Villard, J. W.; *et al.* Small Multifunctional Nanoclusters (Nanoroses) for Targeted Cellular Imaging and Therapy. *ACS Nano* **2009**, *3*, 2686–2696.
11. Wei, Q.; Song, H.-M.; Leonov, A. P.; Hale, J. B.; Oh, D.; Ong, Q. K.; Ritchie, K. P.; Wei, A. Gyromagnetic Imaging: Dynamic Optical Contrast Using Gold Nanostars with Magnetic Cores. *J. Am. Chem. Soc.* **2009**, *131*, 9728–9734.
12. Lyon, J. L.; Fleming, D. A.; Stone, M. B.; Schiffer, P.; Williams, M. E. Synthesis of Fe Oxide Core/Au Shell Nanoparticles by Iterative Hydroxylamine Seeding. *Nano Lett.* **2004**, *4*, 719–723.
13. Wang, L. Y.; Luo, J.; Fan, Q.; Suzuki, M.; Suzuki, I. S.; Engelhard, M. H.; Lin, Y.; Kim, N.; Wang, J. Q.; Zhong, C. J. Monodispersed Core−Shell Fe_3O_4@Au Nanoparticles. *J. Phys. Chem. B* **2005**, *109*, 21593–21601.
14. Park, H.-Y.; Schadt, M. J.; Wang, L. Y.; Lim, I.-I. S.; Njoki, P. N.; Kim, S. H.; Jang, M.-Y.; Luo, J.; Zhong, C.-J. Fabrication of Magnetic Core@Shell Fe Oxide@Au Nanoparticles for

Interfacial Bioactivity and Bio-Separation. *Langmuir* **2007**, *23*, 9050–9056.
15. Pal, S.; Morales, M.; Mukherjee, P.; Srikanth, H. Synthesis and Magnetic Properties of Gold Coated Iron Oxide Nanoparticles. *J. Appl. Phys.* **2009**, *105*, 07B504.
16. Chin, S. F.; Iyer, K. S.; Raston, C. L. Facile and Green Approach To Fabricate Gold and Silver Coated Superparamagnetic Nanoparticles. *Cryst. Growth Des.* **2009**, *9*, 2685–2689.
17. Sun, S. H.; Zeng, H. Size-Controlled Synthesis of Magnetite Nanoparticles. *J. Am. Chem. Soc.* **2002**, *124*, 8204–8205.
18. Sun, S. H.; Zeng, H.; Robinson, D. B.; Raoux, S.; Rice, P. M.; Wang, S. X.; Li, G. Monodisperse MFe_2O_4 (M = Fe, Co, Mn) Nanoparticles. *J. Am. Chem. Soc.* **2004**, *126*, 273–279.
19. Lim, J. K.; Majetich, S. A.; Tilton, R. D. Stabilization of Superparamagnetic Iron Oxide Core−Gold Shell Nanoparticles in High Ionic Strength Media. *Langmuir* **2009**, *25*, 13384–13393.
20. Goon, I. Y.; Lai, L. M. H.; Lim, M.; Munroe, P.; Gooding, J. J.; Amal, R. Fabrication and Dispersion of Gold-Shell-Protected Magnetite Nanoparticles: Systematic Control Using Polyethyleneimine. *Chem. Mater.* **2009**, *21*, 673–681.
21. Levin, C. S.; Hofmann, C.; Ali, T. A.; Kelly, A. T.; Morosan, E.; Nordlander, P.; Whitmire, K. H.; Halas, N. J. Magnetic-Plasmonic Core−Shell Nanoparticles. *ACS Nano* **2009**, *3*, 1379–1388.
22. Marks, L. D. Experimental Studies of Small Particle Structures. *Rep. Prog. Phys.* **1994**, *57*, 603–649.
23. Gatel, C.; Snoeck, E. Epitaxial Growth of Au and Pt on Fe_3O_4(111) Surface. *Surf. Sci.* **2007**, *601*, 1031–1039.
24. Chen, S.; Wang, Z. L.; Ballato, J.; Foulger, S. H.; Carroll, D. L. Monopod, Bipod, Tripod, and Tetrapod Gold Nanocrystals. *J. Am. Chem. Soc.* **2003**, *125*, 16186–16187.
25. Hao, E.; Bailey, R. C.; Schatz, G. C.; Hupp, J. T.; Li, S. Synthesis and Optical Properties of "Branched" Gold Nanocrystals. *Nano Lett.* **2004**, *4*, 327–330.
26. Burt, J. L.; Elechiguerra, J. L.; Reyes-Gasga, J.; Montejano-Carrizales, J. M.; Jose-Yacaman, M. Beyond Archimedean Solids: Star Polyhedral Gold Nanocrystals. *J. Cryst. Growth* **2005**, *285*, 681–691.
27. Xie, J.; Lee, J. Y.; Wang, D. I. C. Seedless, Surfactantless, High-Yield Synthesis of Branched Gold Nanocrystals in HEPES Buffer Solution. *Chem. Mater.* **2007**, *19*, 2823–2830.
28. Liao, H.-G.; Jiang, Y.-X.; Zhou, Z.-Y.; Chen, S.-P.; Sun, S.-G. Shape-Controlled Synthesis of Gold Nanoparticles in Deep Eutectic Solvents for Studies of Structure−Functionality Relationships in Electrocatalysis. *Angew. Chem., Int. Ed.* **2008**, *47*, 9100–9103.
29. Jeong, G. H.; Lee, Y. W.; Kim, M.; Han, S. W. High-Yield Synthesis of Multi-Branched Gold Nanoparticles and Their Surface-Enhanced Raman Scattering Properties. *J. Colloid Interface Sci.* **2009**, *329*, 97–102.
30. Sau, T. K.; Murphy, C. J. Room Temperature, High-Yield Synthesis of Multiple Shapes of Gold Nanoparticles in Aqueous Solution. *J. Am. Chem. Soc.* **2004**, *126*, 8648–8649.
31. Kuo, C.-H.; Huang, M. H. Synthesis of Branched Gold Nanocrystals by a Seeding Growth Approach. *Langmuir* **2005**, *21*, 2012–2016.
32. Wu, H. Y.; Liu, M.; Huang, M. H. Direct Synthesis of Branched Gold Nanocrystals and Their Transformation into Spherical Nanoparticles. *J. Phys. Chem. B* **2006**, *110*, 19291–19294.
33. Nehl, C. L.; Liao, H.; Hafner, J. H. Optical Properties of Star-Shaped Gold Nanoparticles. *Nano Lett.* **2006**, *6*, 683–688.
34. Lu, L.; Ai, K.; Ozaki, Y. Environmentally Friendly Synthesis of Highly Monodisperse Biocompatible Gold Nanoparticles with Urchin-like Shape. *Langmuir* **2008**, *24*, 1058–1063.
35. Kumar, P. S.; Pastoriza-Santos, I.; Rodríguez-González, B.; García de Abajo, F. J.; Liz-Marzán, L. M. High-Yield Synthesis and Optical Response of Gold Nanostars. *Nanotechnology* **2008**, *19*, 015606.
36. Krichevski, O.; Markovich, G. Growth of Colloidal Gold Nanostars and Nanowires Induced by Palladium Doping. *Langmuir* **2006**, *23*, 1496–1499.
37. Hao, F.; Nehl, C. L.; Hafner, J. H.; Nordlander, P. Plasmon Resonances of a Gold Nanostar. *Nano Lett.* **2007**, *7*, 729–732.
38. Xia, Y.; Xiong, Y.; Lim, B.; Skrabalak, S. E. Shape-Controlled Synthesis of Metal Nanocrystals: Simple Chemistry Meets Complex Physics. *Angew. Chem., Int. Ed.* **2009**, *48*, 60–103.
39. Aaron, J. S.; Oh, J.; Larson, T. A.; Kumar, S.; Milner, T. E.; Sokolov, K. V. Increased Optical Contrast in Imaging of Epidermal Growth Factor Receptor Using Magnetically Actuated Hybrid Gold/Iron Oxide Nanoparticles. *Opt. Express* **2006**, *14*, 12930–12943.
40. Oldenburg, A. L.; Toublan, F. J.-J.; Suslick, K. S.; Wei, A.; Boppart, S. A. Magnetomotive Contrast for *In Vivo* Optical Coherence Tomography. *Opt. Express* **2005**, *13*, 6597–6614.
41. Oldenburg, A. L.; Crecea, V.; Rinne, S. A.; Boppart, S. A. Phase-Resolved Magnetomotive OCT for Imaging Nanomolar Concentrations of Magnetic Nanoparticles in Tissues. *Opt. Express* **2008**, *16*, 11525–11539.
42. Liang, X.; Oldenburg, A. L.; Crecea, V.; Chaney, E. J.; Boppart, S. A. Optical Micro-Scale Mapping of Dynamic Biomechanical Tissue Properties. *Opt. Express* **2008**, *16*, 11052–11065.
43. Crecea, V.; Oldenburg, A. L.; Liang, X.; Ralston, T. S.; Boppart, S. A. Magnetomotive Nanoparticle Transducers for Optical Rheology of Viscoelastic Materials. *Opt. Express* **2009**, *17*, 23114–23122.
44. Reed, J.; Ramakrishnan, S.; Schmit, J.; Gimzewski, J. K. Mechanical Interferometry of Nanoscale Motion and Local Mechanical Properties of Living Zebrafish Embryos. *ACS Nano* **2009**, *3*, 2090–2094.
45. Sadtler, B.; Wei, A. Spherical Ensembles of Gold Nanoparticles on Silica: Electrostatic and Size Effects. *Chem. Commun.* **2002**, 1604–1605.
46. Zhao, Y.; Sadtler, B.; Min, L.; Hockerman, G. H.; Wei, A. Nanoprobe Implantation into Mammalian Cells by Cationic Transfection. *Chem. Commun.* **2004**, 784–785.
47. Wei, Q.; Wei, A. In *The Supramolecular Chemistry of Organic-Inorganic Hybrid Materials*; Rurack, K., Martínez-Mañez, R., Eds.; John Wiley and Sons: New York, 2010; pp 319−349.
48. Leonov, A. P.; Zheng, J.; Clogston, J. D.; Stern, S. T.; Patri, A. K.; Wei, A. Detoxification of Gold Nanorods by Treatment with Polystyrenesulfonate. *ACS Nano* **2008**, *2*, 2481–2488.
49. Pol, A.; Ortega, D.; Enrich, C. Identification of Cytoskeleton-Associated Proteins in Isolated Rat Liver endosomes. *Biochem. J.* **1997**, *327*, 741–746.
50. Styers, M. L.; Salazar, G.; Love, R.; Peden, A. A.; Kowalczyk, A. P.; Faundez, V. The Endo-Lysosomal Sorting Machinery Interacts with the Intermediate Filament Cytoskeleton. *Mol. Biol. Cell* **2004**, *15*, 5369–5382.
51. Richards, C. I.; Hsiang, J.-C.; Senapati, D.; Patel, S.; Yu, J.; Vosch, T.; Dickson, R. M. Optically Modulated Fluorophores for Selective Fluorescence Signal Recovery. *J. Am. Chem. Soc.* **2009**, *131*, 4619–4621.
52. Richards, C. I.; Hsiang, J.-C.; Khalil, A. M.; Hull, N. P.; Dickson, R. M. FRET-Enabled Optical Modulation for High Sensitivity Fluorescence Imaging. *J. Am. Chem. Soc.* **2010**, *132*, 6318–6323.